

Published in final edited form as:

J Instrum. 2011 December ; 6(12): . doi:10.1088/1748-0221/6/12/C12009.

Pixellated Cd(Zn)Te high-energy X-ray instrument

P. Seller^{a,1}, S. Bell^a, R.J. Cernik^b, C. Christodoulou^c, C.K. Egan^b, J.A. Gaskin^f, S. Jacques^b, S. Pani^d, B.D. Ramsey^f, C. Reid^c, P.J. Sellin^d, J.W. Scuffham^{d,e}, R.D. Speller^c, M.D. Wilson^a, and M.C. Veale^a

^aTechnology Department, Rutherford Appleton Laboratory, Harwell Science and Innovation Campus, Didcot, OX110QX, U.K.

^bSchool of Materials, Manchester University, Grosvenor St., Manchester, M1 7HS, U.K.

^cDepartment of Medical Physics and Bioengineering, University College London, Malet Place Engineering Building, London, WC1E6BT, U.K.

^dDepartment of Physics, University of Surrey, Guildford, GU2 7XH, U.K.

^eNuclear Medicine Department, Royal Surrey County Hospital, Egerton Road, Guildford, GU2 7XX, U.K.

^fNASA Space Science Technology Centre 320 Sparkman Drive, Huntsville, AL 35805, U.S.A.

Abstract

We have developed a pixellated high energy X-ray detector instrument to be used in a variety of imaging applications. The instrument consists of either a Cadmium Zinc Telluride or Cadmium Telluride (Cd(Zn)Te) detector bump-bonded to a large area ASIC and packaged with a high performance data acquisition system. The 80 by 80 pixels each of 250 μm by 250 μm give better than 1 keV FWHM energy resolution at 59.5 keV and 1.5 keV FWHM at 141 keV, at the same time providing a high speed imaging performance. This system uses a relatively simple wire-bonded interconnection scheme but this is being upgraded to allow multiple modules to be used with very small dead space. The readout system and the novel interconnect technology is described and how the system is performing in several target applications.

Keywords

X-ray detectors; Pixelated detectors and associated VLSI electronics; X-ray detectors and telescopes; Gamma camera; SPECT; PET PET/CT; coronary CT angiography (CTA)

1 Introduction

Cadmium Telluride and Cadmium Zinc Telluride Cd(Zn)Te based detectors have become the best prospect for room-temperature X-ray detectors. They are being used for commercial applications in medical, security and science applications. Commercially supplied material and subsequent detector processing have improved considerably over the last few years [1, 2] but there are intrinsic X-ray conversion properties and charge transport properties that have to be addressed in order to make useful imaging and spectroscopy devices [3]–[5]. There is also an issue with the available and practical size of single detector segments. CdTe devices seem to be available in many cm square devices but CdZnTe single crystals seem to

be currently limited to 20mm×20mm. Also the thermal mismatch issues between Cd(Zn)Te and silicon poses problems for bonding of fine pitch imaging devices.

Our collaboration has built a readout system for fine pitch Cd(Zn)Te detectors suitable for imaging and spectroscopy [6, 7]. We are using this in several novel applications with 20 mm×20 mm devices and are building mechanics and readout for creating larger area segmented arrays.

We refer to Cd(Zn)Te where the distinction between Cadmium Telluride and Cadmium Zinc Telluride is not important but use CdTe or CdZnTe where we wish to be specific.

2 X-ray conversion and charge transport issues

Cd(Zn)Te detectors typically need to be from 1 to 3 mm thick for X-ray imaging applications to have good efficiency up to a few hundred keV photons. With 400V to 1kV applied to the detector a single spot of charge carriers generated by radiation will diffuse out to 100–200 μm as they drift across the detector [8]–[10]. With small pixels this can cause significant charge sharing between pixel pads. With very small pixels of 50 μm the charge sharing is extreme and reconstruction of the event is difficult [10, 11]. This causes significant complexity in reconstructing the signal to produce good spectroscopy. Also absorbed X-rays above the k-edge of Cd and Te produce fluorescence photons which have a range of about 60 μm in Cd(Zn)Te. This also has a significant effect on imaging and spectroscopy with small pixels. There is a significant trapping of charge carriers in all Cd(Zn)Te. Holes have a lower mobility in Cd(Zn)Te than electrons which leads to lower $\mu\tau$ -product [12, 13]. The effect of this is that X-rays generated at different depths in a device produce different induced charges. This causes low energy ‘tailing’ in the spectra produced from the device. One of several methods to reduce this effect is to use the small pixel effect which can be used to effectively make the device single carrier (electron) sensitive [14, 15].

From these arguments we have come to a compromise between small pixels for low tailing, and large enough pixels to allow efficient inter-pixel-sharing processing to be achievable. Additional considerations for choosing the pixel size was that the gold stud bonding that we use requires a large 60 μm bond pad on the ASIC and also we chose a relatively coarse 0.35 μm CMOS process as we need full engineering processing runs. A deep sub-micron process would be very expensive. Also integration of the very low noise circuitry in the pixel requires large components which constrained us to the 250 μm pixel. In summary we have chosen 250 μm pixel pitch as a compromise which also allows us to integrate the low-noise electronics and connect via a simple low cost bump bonding process. Possibly a 200 μm pixels would have been optimal if we had more space in the ASIC pixel. With this geometry we typically have 40% of events which are shared between pixels [16, 17]. For this case we can either add the signals together or if efficiency is not a problem we can just reject shared events. Figure 1 shows a 3 mm thick CdZnTe detector bump bonded to an 80×80 pixel readout ASIC with the RAL technique of gold studs on the ASIC and silver loaded epoxy dispensed dots on the Cd(Zn)Te. The I/O pads of the ASIC are then aluminium wire bonded to the readout board.

3 Readout ASIC and data acquisition system

A 20 pixel by 20 pixel test structure has been described before [6]. This has a rolling shutter architecture so that the 20 column outputs of each of the 20 rows are sent sequentially to an analogue multiplexer for serial output to an off-chip 20MHz 12bit ADC. In the 8080 ASIC the number of rows is expanded to 80 rows so that the 20 columns outputs of each of the 80 rows are sent sequentially to an ADC. This structure is then repeated 4 times on the ASIC so that there are 4 banks of columns each connected to a 20 element multiplexer with its own

analogue output. The 4 outputs allow the ASIC to output 4 times faster than having just one output. The ASIC operates continuously so that the whole ASIC is readout in $20 \times 80 \times 50$ ns plus some extra clock cycles for data alignment. Effectively the whole ASIC is readout on the 4 outputs at about 10,000 frames per second.

The pixel circuitry of the 8080 device is identical to the 2020 device where each pixel has a preamplifier followed by a $2 \mu\text{s}$ CR-RC shaper and a peak-track-and-hold circuit. This circuit stores the peak value of the largest signal that occurs in the frame time. The signal represents the charge deposited in the detector and is thus proportional to the energy of the single photon stopping in the detector. This analogue voltage is held till the end of the frame where it is transferred to the row output. Only the largest energy photon in each frame is readout of each pixel. On the edge of the ASIC there are 3 column and 3 row registers. These are serially programmed and allow a row or column to have a calibrate signal applied, be switched into low power mode or to skip readout. The low power mode reduces the power on the ASIC but increases noise and skipping readout allows a faster frame time as less clocks are used to read a frame. The ASIC was built on AMS $0.35 \mu\text{m}$ CMOS process and is $20 \text{ mm} \times 22 \text{ mm}$ which is close to the maximum reticule size achievable.

Programming of the serial registers and sequencing the row clocks and multiplexer clocks is performed by an FPGA local to the ASIC. The digitised Peak-Track-and-Hold outputs from the 4 ADCs are packaged locally by the FPGA and sent by Camera-Link to a frame grabber in the Control PC. The FPGA, ADCs and Camera-Link driver is situated on a local stack of boards which is packaged in a metal enclosure (shown in figure 2) together with a PID Peltier driven temperature control system. This system stabilises the temperature of the ASIC and Cd(Zn)Te detector to better than 1 degree in a range from 10C to 30C. This is particularly important to stabilise pedestal shifts in the ASIC, together with leakage current and trapping in the detector. The system controls the temperature of a copper block in the system. The cards which contain the ASIC and detector have a copper insert which pushes against this copper block to transfer the heat from the ASIC. This allows detectors to be conveniently exchanged in the system. The 8080 ASIC has an on-chip temperature monitoring circuit to record the temperature during operation.

The metal enclosure has mounting points to connect to standard optical mounting rails. This allows the detector to be aligned and scanned in experimental runs.

4 Measured performance

4.1 CdTe image and performance

An 80×80 pixel piece of 1 mm thick CdTe from Acrorad was gold stud and silver epoxy [17, 18] bump bonded to an 8080 ASIC. The pixellated contact on the anode was aluminum, which forms a Schottky contact to suppress the leakage current from the bulk but doesn't diffuse into the CdTe material and cause the pixels to short together [19].

The detector was biased to -500 V and held at a constant temperature of 20°C for a 6 hours exposure. Figure 3 shows the image of photons from a partially collimated Am-241 source. Note that the image is not uniform in intensity due to the geometry of the source, not the efficiency of the detector. The red area is the high flux region from the partially collimated source. To avoid polarisation [20] the bias was refreshed to 0 V for 2 s once every 60 s. The data from the detector was processed using a charge sharing discrimination correction where any charge sharing events were removed from the data [7, 16]. The Am-241 peak at 59.5 keV and the Np (Am daughter product) peaks at 13.9, 17.8 and 20.8 keV were used to give a linear calibration to each pixel separately. Figure 3 shows the number of events per pixel (left) and a spectrum from a typical single pixel (right). The pixel intensity map has had the

edge pixel removed and a dead row of pixels has been corrected. The bump bonding yield was > 99.9% and the isolated dark blue or black pixels are pixels with low collection efficiency that are believed to be related to CdTe crystal defects. In practice such isolated pixels would be corrected by interpolation of neighboring pixels. The energy spectrum from a typical pixel has the main Am-241 peak at 59.5 keV with a low energy shoulder down to 56 keV which is caused by a combination of charge trapping and charge sharing events where the low energy fraction of the shared event is not detected as it is below the 4 keV low energy threshold of the detector. The Np lines, Te and Cd characteristic lines and escape peaks are also clearly resolved in the spectrum.

Good spectral performance has previously been demonstrated with 1 mm thick CdTe with the 20×20 pixel test structure but these results show that the spectral performance is maintained in the larger 80×80 pixel device (20 mm× 20 mm active area) [21]. Figure 4 shows that the majority of pixels have a FWHM at 59.5 keV of less than 1 keV and many pixels achieve 800eV FWHM which is comparable performance to the Amptek single element CdTe diodes [22]. The average of the distribution of FWHM for all active pixels was 0.87 keV with an rms of the distribution of FWHM of 0.34 keV. By comparing the intensity maps for the number of events in figure 3 and the FWHM in figure 4 it is clear that there are more pixels with a relatively high FWHM (> 1.5 keV) than pixels that have a low collection efficiency. There is some correlation of the low efficiency pixels with high noise pixels but it is by no means an exact match. This might be due to different defects in the CdTe material that could cause charge trapping or charge-steering away from some pixels to give low efficiency pixels. Also some defects cause partial charge trapping that result in degraded energy resolution. Detailed investigations into the cause, characterisation and effect of traps in Cd(Zn)Te have been studied elsewhere and further analysis of these defects is beyond the scope of this paper [23, 24].

4.2 CdTe at high energies

The 80×80 detector has applications with energies up to 160 keV. One of these applications is multiple isotopes SPECT where two or more radio-isotopes are imaged simultaneously and the energy spectra are used to separate the image components from the different sources [25, 26]. An early trial was conducted with a Tc-99m point source and a different 1 mm thick Al-Schottky CdTe detector used to collect the Am-241 data. The detector was held at 25°C and -500 V applied for 60s and 0 V applied for 2 s. A 0.1 ml syringe of the 10 MBq source was used as a source.

The raw data was processed with charge sharing discrimination and calibrated using the Tc-99m peaks at 141 keV, 18 keV and 21 keV as well as the Cd escape peak at 118 keV. The spectrum from a typical single pixel shown in figure 5 shows each of these peaks with some other characteristic lines, escape peaks and a small noise continuum around 90–110 keV from back and Compton scattering. As with the Am-241 spectrum, there is a low energy shoulder to the main peak at 141 keV which is mainly due to charge sharing events where the low energy fraction of the shared event is not detected as it is below the low energy threshold of the detector. The noise edge out to 10 keV is believed to be due to scattered events. The FWHM of the 141 keV peak was measured for all active pixels; the distribution of the FWHM per pixel is shown in figure 5. The average FWHM at 141 keV was 1.1 keV (0.78%) with an rms of 0.2 keV.

Although the 1 mm thick CdTe has demonstrated excellent spectral resolution throughout the energy range of the 8080 ASIC it is limited in efficiency as less than 40% of 141 keV gamma rays will be absorbed in the devices [27]. The solution to this would be to use thicker CdTe, but thicker Schottky CdTe polarizes very quickly and Ohmic contact CdTe cannot be used as it gives much higher leakage currents. CdZnTe does not suffer from bias

induced polarization and can be manufactured with increased thickness [1]. This does not require bias refreshing and thick detectors give higher efficiency at high energies. Good spectral performance has been achieved with 2 mm thick travelling heater method grown CdZnTe on the 20×20 pixel test detectors [7, 21] but it is not readily available with our fine pixelation. It is worth noting that without depth of interaction corrections using thicker detector material will inherently cause a small degradation in the spectral performance of the detector as the charge carrier clouds will have a longer drift length and will be more likely to encounter a material defect. We have measured 2 mm thick CdZnTe, 20×20 pixel devices giving FWHM < 1.5 keV at 59.5 keV. If this performance could be repeated on larger area CdZnTe detectors then it would be more than adequate for most high energy applications and give higher efficiency.

5 Applications

The instrument described here images the X-rays incident on the 80×80 pixel detector and also measures the energy of every photon arriving with better than 1.5 keV FWHM. This combination of X-ray imaging and good spectroscopic information has not been available to applications before and thus presents new measurement possibilities. The authors are developing several applications using the instrument:

- **Energy Dispersive Diffraction Imaging of Cancerous Tissues:** Cancerous breast tissue diffracts X-rays to a different extent than normal tissue due to the different structure of collagen and adipose tissues. We are using the combined spectral and position resolution to use white beam to measure momentum transfer patterns of the X-rays [28]. This technique could potentially lead to tissue identification during operations to aid surgical removal of exactly the correct amount of tumour bed.
- **Energy Dispersive Diffraction Imaging of Illicit Substances:** Illicit drugs and solid explosives have well characterised X-ray diffraction signatures. We are using white beam illuminated samples to perform the diffraction measurement and multivariate analysis techniques to improve the sensitivity and specificity of the identification [29, 30].
- **Materials Characterisation Techniques:** By selecting and spatially mapping X-ray fluorescence signals stimulated from solid materials we can perform materials specific imaging where individual elemental species can be directly mapped. [31]. An example of an application of this technique is shown in figure 6, where we study the spatial distribution of elemental species in an industrial catalyst. The catalyst in question is a 3 mm diameter alumina sphere loaded with a low percentage of Pt (0.1 %). These catalyst bodies are loaded, in thousands, into fixed-bed catalytic reactors. The particular catalyst has been used in hydrocarbon cracking, and undergone poisoning by Sb present in the hydrocarbon stream. The amount and extent of the poisoning is crucial knowledge for improving industrial catalytic processes, for example how far does the poison penetrate and what is the spatial distribution? In this case, we can see the Sb clearly shows an egg-shell distribution penetrating about 0.5 mm into the alumina sphere. Whilst in this particular example the sample could have been examined by traditional sectioning and EDX analysis, our results show that the method offers the opportunity to perform *in operando* imaging on short time-scales.
- **Astrophysics & Solar Imaging and Spectroscopy:** X-ray astronomy and solar spectroscopic imaging telescopes typically employ grazing incidence optics to focus X-rays onto a detector located at the focal plane. The implementation of high-resolution, hard-X-ray (up to ~80 keV) focusing optics necessitates a corresponding high-spatial resolution detector that can oversample the mirror

response function, to realize the full system angular resolution, while providing the keV-level energy resolution necessary for spectral line and continuum measurements [32]. We are currently in the process of preparing 2x2 CdTe pixellated detector arrays for the balloon flight mission Super-HERO, to replace the high-pressure Xe gas-scintillation-proportional counters currently being used. Once these focal-plane detector arrays are coupled to the X-ray optics, developed at NASA Marshall Space Flight Center, Super-HERO will be able to make the highest-imaging-resolution hard X-ray observations to date.

- ***Simultaneous Dual Isotope Nuclear Medical Imaging:*** Gamma camera SPECT systems routinely use isotopes such as Tc-99m and I-123 (gamma emissions of 141 keV and 159 keV respectively) to produce images of physiological function. There is a growing interest in the use of multiple tracers to image different biological processes simultaneously to aid in the differential diagnosis of disease [25, 26, 33]. The improved energy resolution offered by semiconductor detectors has already facilitated this in the field of cardiology. There are also potential applications in neurology, where simultaneous imaging of brain perfusion (Tc-99m) and dopamine transporters (I-123) can help to differentiate Parkinson's disease from Multiple System Atrophy. In this application, both high spatial- and energy resolution is required, and The Royal Surrey County Hospital is developing a solid-state detector system for this purpose as part of the HEXITEC collaboration.
- ***K-Edge Absorption Imaging by Scanning and Cone Beam Projection:*** We have done initial trials for use as identification of cancerous tissue samples with Iodine as a K-edge absorbing contrast agent at 33 keV [34].

6 Tiled arrays

As explained earlier there are applications where larger areas are needed than the existing 20 mm x 20 mm devices. There is a problem in bonding larger area devices due to the significant Coefficient of Thermal Expansion mismatch between Cd(Zn)Te and the silicon readout ASIC. The other issue is the availability and cost of large area Cd(Zn)Te devices. We are addressing this problem by mounting the 8080 devices on small Aluminium carriers. These carriers are then accurately aligned to a copper cooling block which is connected to the cooled copper block in the metal enclosure.

Figure 7 shows how 4 devices can be mounted together and how the wire bonded I/O connections from the ASICs are routed through small 'door-step' cards to connectors on the back of the carriers. The ASICs are built to be 3 side buttable on the 250 μm pitch so that in principle we can extend this to a 2xn arrangement. The carriers are built so that we can mount ASICs and detectors to an accuracy of 100 μm . This will allow very small gaps in between detectors. Our existing detectors are built with 250 μm guard bands on all sides. We are currently investigating the effect of reducing or removing the guard bands, specifically looking at how this will affect spectroscopy of the edge pixels. The standard detectors that we use currently will have no difference in performance between multiple or single detectors.

7 Summary

We have built an 80 by 80 pixel Cd(Zn)Te based X-ray detector instrument capable of imaging and spectroscopy. The instrument operates at up to 10,000 frames per second while giving 250 μm resolution and < 1.5 keV FWHM performance up to 160 keV. Individual detector blocks can be tiled in a 2xn arrangement to increase the imaging area with small inter-detector dead regions.

Acknowledgments

We acknowledge the funding contribution from UK EPSRC via the Hexitec grant EP/D048737/1. We also thank the STFC contribution of L.L. Jones and S.L. Thomas who designed the 8080 ASIC and Paul Adkin and Paul Booker for bonding the detectors.

References

- [1]. Amman MA, Lee JS, Luke PN, Chen H, Awadalla SA, Redden R, Bindley G. Evaluation of THM-Grown CdZnTe Material for Large-Volume Gamma-Ray Detector Applications. *IEEE T. Nucl. Sci.* 2009; 56:795.
- [2]. Shiraki H, Funaki M, Ando Y, Kominami S, Amemiya K, Ohno R. Improvement of the Productivity in the THM Growth of CdTe Single Crystal as Nuclear Radiation Detector. *IEEE T. Nucl. Sci.* 2010; 57:395.
- [3]. Sellin PJ, et al. Ion beam induced charge imaging of charge transport in CdTe and CdZnTe. *Nucl. Instrum. Meth. B.* 2008; 266
- [4]. Szeles C. CdZnTe and CdTe materials for X-ray and gamma ray radiation detector applications. *Phys. Status Solidi B.* 2004; 241:7830.
- [5]. He Z, Knoll GF, Wehe DK. Direct measurement of product of the electron mobility and mean free drift time of CdZnTe semiconductors using position sensitive single polarity charge sensing detectors. *J. App. Phys.* 1998; 84:5566.
- [6]. Jones L, Seller P, Wilson M, Hardie A. HEXITEC ASIC—a pixellated readout chip for CZT detectors. *Nucl. Instrum. Meth. A.* 2009; 604:34.
- [7]. Wilson MD, et al. Small pixel CZT detector for hard X-ray spectroscopy. *Nucl. Instrum. Meth. A.* 2011; 652:158.
- [8]. Benoit M, Hamel LA. Simulation of charge collection processes in semiconductor CdZnTe [gamma]-ray detectors. *Nucl. Instrum. Meth. A.* 2009; 606:508.
- [9]. Meuris A, Limousin O, Blondel C. Charge sharing in CdTe pixilated detectors. *Nucl. Instrum. Meth. A.* 2009; 610:294.
- [10]. Gimenez EN, et al. Study of charge-sharing in MEDIPIX3 using a micro-focused synchrotron beam. *JINST.* 2011; 6:C01031.
- [11]. Pellegrini G, et al. Performance limits of a 55 μm pixel CdTe detector. *IEEE Nucl. Sci. Symp. Conf.* 2004; 4:2104.
- [12]. Suzuki K, Seto S, Sawada T, Imai K. Carrier transport properties of HPB CdZnTe and THM CdTe:Cl. *IEEE T. Nucl. Sci.* 2002; 49:1287.
- [13]. Veale MC, Sellin PJ, Parkin JM, Lohstroh A, Davies AW, Seller P. Ion Beam Induced Charge Studies of CdZnTe Grown by Modified Vertical Bridgman Method. *IEEE T. Nucl. Sci.* 2008; 55:3741.
- [14]. He Z. Review of the Shockley–Ramo theorem and its application in semiconductor gamma-ray detectors. *Nucl. Instrum. Meth. A.* 2001; 463:250.
- [15]. Wilson MD, Seller P, Veale MC, Sellin PJ. Investigation of the small pixel effect in CdZnTe detectors. *IEEE Nucl. Sci. Symp. Conf. Rec.* 2007; 2:1255.
- [16]. Veale MC. An ASIC for the Study of Charge Sharing Effects in Small Pixel CdZnTe X-Ray Detectors. *IEEE T. Nucl. Sci.* 2011; 58:2357. at al.
- [17]. Castilla J, et al. Development of a 24×24 CZT-FEE pixel detector block for the CSTD project. *IEEE Nucl. Sci. Symp. Conf. Rec.* 2008; 1:254.
- [18]. Clayton JE, Chen CMH, Cook WR, Harrison FA. Assembly technique for a fine-pitch, low-noise interface; Joining a CdZnTe pixel-array detector and custom VLSI chip with Au stud bumps and conductive epoxy. *IEEE Nucl. Sci. Symp. Conf.* 2003; 5:3513.
- [19]. Watanabe S, et al. High Energy Resolution Hard X-Ray and Gamma-Ray Imagers Using CdTe Diode Devices. *IEEE T. Nucl. Sci.* 2009; 56:777.
- [20]. Niraula M, Nakamura A, Aoki T, Tomita Y, Hatanaka Y. Stability issues of high-energy resolution diode type CdTe nuclear radiation detectors in a long-term operation. *Nucl. Instrum. Meth. A.* 2002; 491:168.

- [21]. Wilson MD, et al. Comparison of the X-ray performance of small pixel CdTe and CZT detectors. IEEE Nucl. Sci. Symp. Conf. Rec. 2010; 1:3942.
- [22]. Takahashi T, Watanabe S. Recent progress in CdTe and CdZnTe detectors. IEEE T. Nucl. Sci. 2001; 48:950.
- [23]. Bolotnikov AE, et al. Extended Defects in CdZnTe Radiation Detectors. IEEE T. Nucl. Sci. 2009; 56:1775.
- [24]. Schlesinger T, et al. Cadmium zinc telluride and its use as a nuclear radiation detector material. Mat. Sci. Eng. R. 2001; 32:103.
- [25]. Ben-Haim S, et al. Simultaneous dual-radionuclide myocardial perfusion imaging with a solid-state dedicated cardiac camera. Eur. J. Nucl. Med. Mol. I. 2010; 37:1710.
- [26]. Wagenaar DJ, et al. In Vivo Dual-Isotope SPECT Imaging with Improved Energy Resolution. IEEE Nucl. Sci. Symp. Conf. Rec. 2006; 6:3821.
- [27]. Hubbell, JH.; Seltzer, SM. Tables of X-Ray Mass Attenuation Coefficients and Mass Energy-Absorption Coefficients. version 1.4. National Institute of Standards and Technology; Gaithersburg, MD, U.S.A.: <http://physics.nist.gov/xaamdi>
- [28]. Griffiths JA, Royle GJ, Horrocks JA, Hanby AM, Pani S, Speller RD. Angular dispersive diffraction microCT of small breast tissue samples. Radiat. Phys. Chem. 2007; 77:373.
- [29]. Cook EJ, Pani S, George L, Hardwick S, Horrocks JA, Speller RD. Multivariate Data Analysis for Drug Identification Using Energy-Dispersive X-Ray Diffraction. IEEE T. Nucl. Sci. 2009; 56:1459.
- [30]. Cook E, Fong R, Horrocks J, Wilkinson D, Speller R. Energy dispersive X-ray diffraction as a means to identify illicit materials: A preliminary optimisation study. Appl. Radiat. Isotopes. 2007; 65:959.
- [31]. Beale AM, Jacques SDM, Bergwerff JA, Barnes P, Weckhuysen BM. Tomographic energy dispersive diffraction imaging as a tool to profile in three dimensions the distribution and composition of metal oxide species in catalyst bodies. Angew. Chem. Int. Edit. 2007; 46:8832.
- [32]. Ramsey BD, et al. HERO: high-energy replicated optics for a hard-x-ray balloon payload. Proc. SPIE. 2000; 4138:147.
- [33]. Fakhri G, et al. Quantitative simultaneous ^{99m}Tc -ECD/ ^{123}I -FP-CIT SPECT in Parkinson's disease and multiple system atrophy. Eur. J. Nucl. Med. Mol. I. 2006; 33:87.
- [34]. Pani S, et al. K-edge subtraction imaging using a pixellated energy-resolving detector. Proc. SPIE. 2011; 7961:79614C.

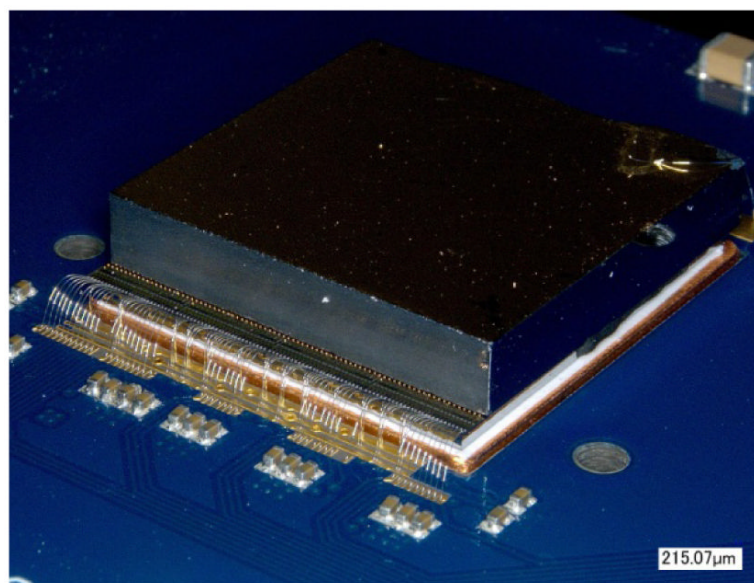


Figure 1.
A 20 mm×20 mm×3 mm CdZnTe detector bump bonded to the 80*80 readout ASIC.

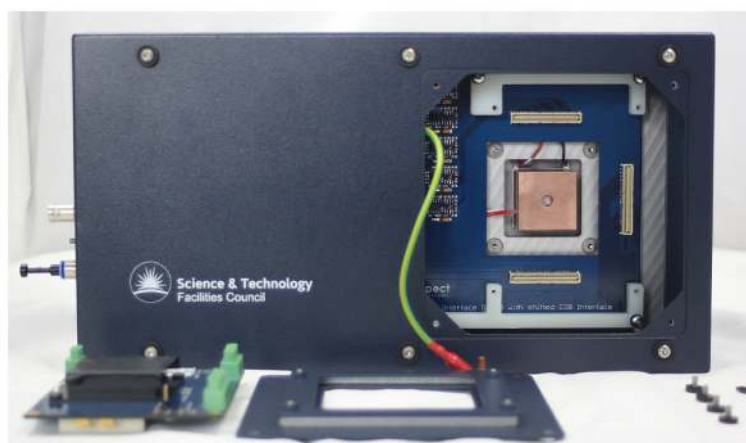


Figure 2.
Enclosure with readout and temperature stabilisation, see detector board lower left.

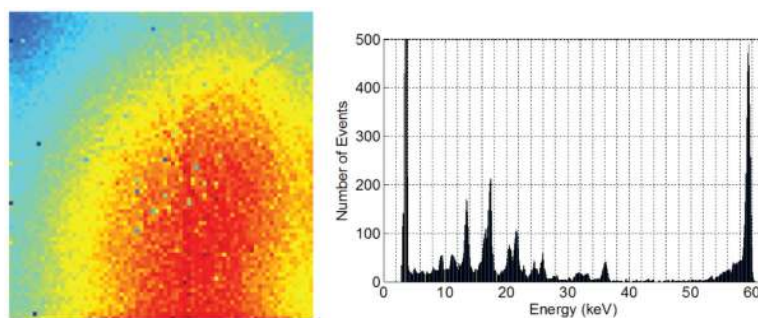


Figure 3.
An image of X-rays from an Am-241 sealed source showing the number of events per pixel (left) and the Am-241 spectrum from a typical pixel (right).

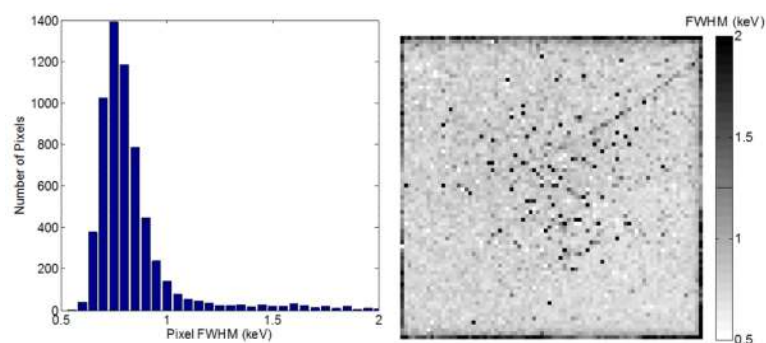


Figure 4.
The distribution of the FWHM of the 59.5 keV peak for all single pixels (left) and the spatial variation in FWHM per pixel (right).

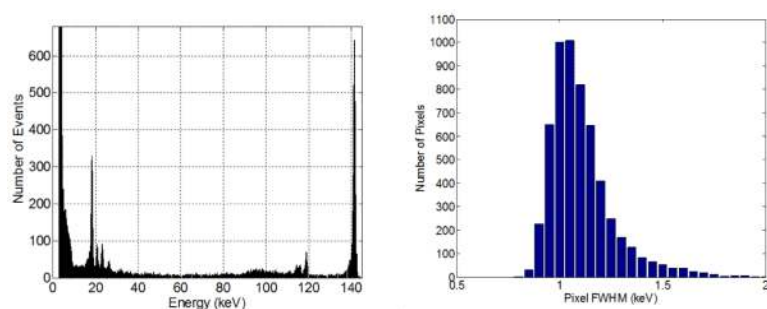


Figure 5.

A Tc-99m spectrum spectrum collected on a single pixel (left) and the distribution of the FWHM of the 141 keV peak measured on each pixel.

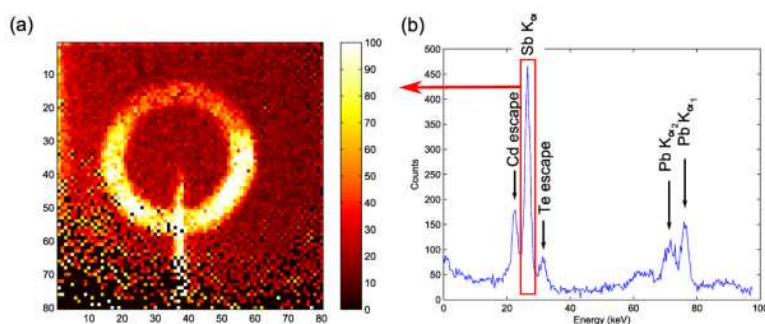


Figure 6.

A XRF imaging of a catalytic body. a) Spatial distribution of the Sb fluorescence peak. b) Individual spectrum showing Sb and Pb fluorescence peaks, the later being present due to extraneous signal from the beam stop. A vertical 100 micron X-ray beam was used to image a slice through the centre of the catalyst body with the image formed using a pinhole camera.

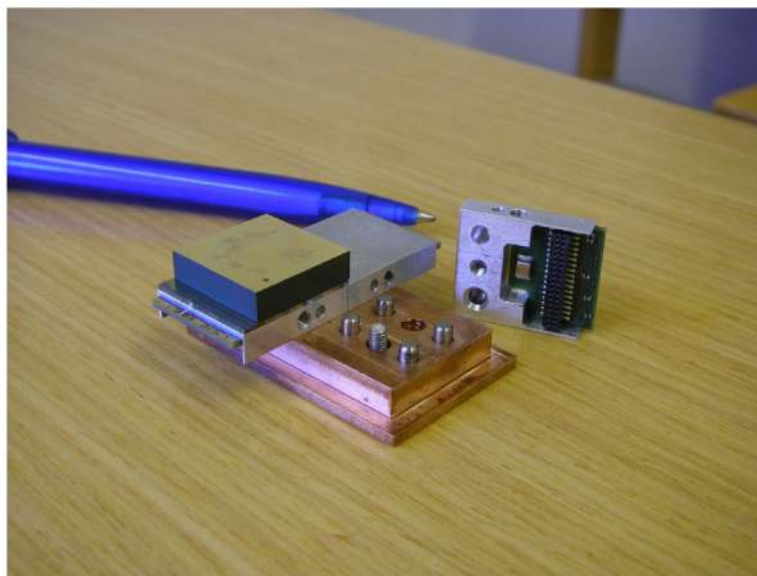


Figure 7. Aluminium carriers on copper alignment block. The carrier has alignment holes, 'door-step' card and connector which is wire bonded to the ASIC I/O pads. A 5 mm thick CdZnTe detector is shown for demonstration.